

# The Heavy Photon Search Test Detector

M. Battaglieri<sup>a</sup>, S. Boyarinov<sup>b</sup>, S. Bueltmann<sup>c</sup>, V. Burkert<sup>b</sup>, W. Cooper<sup>d</sup>, C. Cuevas<sup>b</sup>, N. Dashyan<sup>e</sup>, R. DeVita<sup>a</sup>, C. Desnault<sup>f</sup>, A. Deur<sup>b</sup>, H. Egiyan<sup>b</sup>, L. Elouadrhiri<sup>b</sup>, R. Essig<sup>g</sup>, V. Fadeyev<sup>h</sup>, C. Field<sup>i</sup>, A. Freyberger<sup>b</sup>, Y. Gershtein<sup>j</sup>, N. Gevorgyan<sup>e</sup>, F.-X. Girod<sup>b</sup>, N. Graf<sup>i</sup>, M. Graham<sup>i</sup>, K. Griffioen<sup>k</sup>, A. Grillo<sup>h</sup>, M. Guidal<sup>f</sup>, G. Haller<sup>i</sup>, P. Hansson Adrian<sup>i,\*</sup>, R. Herbst<sup>i</sup>, M. Holtrop<sup>l</sup>, J. Jaros<sup>i</sup>, S. Kaneta<sup>b</sup>, M. Khandaker<sup>m</sup>, A. Kubarovskiy<sup>n</sup>, V. Kubarovskiy<sup>b</sup>, T. Maruyama<sup>i</sup>, J. McCormick<sup>i</sup>, K. Moffeit<sup>i</sup>, O. Moreno<sup>h</sup>, H. Neal<sup>i</sup>, T. Nelson<sup>i</sup>, S. Niccolai<sup>f</sup>, A. Odian<sup>i</sup>, M. Oriunno<sup>i</sup>, R. Paremuzyan<sup>e</sup>, R. Partridge<sup>i</sup>, S. K. Phillips<sup>l</sup>, E. Rauly<sup>f</sup>, B. Raydo<sup>b</sup>, J. Reichert<sup>i</sup>, E. Rindel<sup>f</sup>, P. Rosier<sup>f</sup>, C. Salgado<sup>m</sup>, P. Schuster<sup>o</sup>, Y. Sharabian<sup>b</sup>, D. Sokhan<sup>p</sup>, S. Stepanyan<sup>b</sup>, N. Toro<sup>o</sup>, S. Uemura<sup>i</sup>, M. Ungaro<sup>b</sup>, H. Voskanyan<sup>e</sup>, D. Walz<sup>i</sup>, L. B. Weinstein<sup>c</sup>, B. Wojtsekhowski<sup>b</sup>

<sup>a</sup>Istituto Nazionale di Fisica Nucleare, Sezione di Genova e Dipartimento di Fisica dell'Università, 16146 Genova, Italy

<sup>b</sup>Thomas Jefferson National Accelerator Facility, Newport News, Virginia 23606

<sup>c</sup>Old Dominion University, Norfolk, Virginia 23529

<sup>d</sup>Fermi National Accelerator Laboratory, Batavia, IL 60510-5011

<sup>e</sup>Yerevan Physics Institute, 375036 Yerevan, Armenia

<sup>f</sup>Institut de Physique Nucléaire d'Orsay, IN2P3, BP 1, 91406 Orsay, France

<sup>g</sup>Stony Brook University, Stony Brook, NY 11794-3800

<sup>h</sup>University of California, Santa Cruz, CA 95064

<sup>i</sup>SLAC National Accelerator Laboratory, Menlo Park, CA 94025

<sup>j</sup>Rutgers University, Department of Physics and Astronomy, Piscataway, NJ 08854

<sup>k</sup>The College of William and Mary, Department of Physics, Williamsburg, VA 23185

<sup>l</sup>University of New Hampshire, Department of Physics, Durham, NH 03824

<sup>m</sup>Norfolk State University, Norfolk, Virginia 23504

<sup>n</sup>Rensselaer Polytechnic Institute, Department of Physics, Troy, NY 12181

<sup>o</sup>Perimeter Institute, Ontario, Canada N2L 2Y5

<sup>p</sup>University of Glasgow, Glasgow, G12 8QQ, Scotland, UK

---

## Abstract

The Heavy Photon Search (HPS), an experiment to search for a hidden sector photon in fixed target electroproduction, is preparing for installation at the Thomas Jefferson National Accelerator Facility (JLab) in the Fall of 2014. As the first stage of this project, the HPS Test Run apparatus was constructed and operated in 2012 to demonstrate the experiment's technical feasibility and to confirm that the trigger rates and occupancies are as expected. This paper describes the HPS Test Run apparatus and readout electronics and its performance. In this setting, a heavy photon can be identified as a narrow peak in the  $e^+e^-$  invariant mass spectrum, above the trident background or as a narrow invariant mass peak with a decay vertex displaced from the production target, so charged particle tracking and vertexing are needed for its detection. In the HPS Test Run, charged particles are measured with a compact forward silicon microstrip tracker inside a dipole magnet. Electromagnetic showers are detected in a PbWO<sub>4</sub> crystal calorimeter situated behind the magnet, and are used to trigger the experiment and identify electrons and positrons. Both detectors are placed close to the beam line and split top-bottom. This arrangement provides sensitivity to low-mass heavy photons, allows clear passage of the unscattered beam, and avoids the spray of degraded electrons coming from the target. The discrimination between prompt and displaced  $e^+e^-$  pairs requires the first layer of silicon sensors be placed only 10 cm downstream of the target. The expected signal is small, and the trident background huge, so the experiment requires very large statistics. Accordingly, the HPS Test Run utilizes high-rate readout and data acquisition electronics and a fast trigger to exploit the essentially 100% duty cycle of the CEBAF accelerator at JLab.

**Keywords:** silicon, microstrip, tracking, vertexing, heavy photon, dark photon, hidden sector, electromagnetic calorimeter

---

---

\*Corresponding author.  
*Email address:* phansson@slac.stanford.edu (P. Hansson  
Adrian)

1    **1. Introduction**

2    The heavy photon ( $A'$ ), aka a “hidden sector” or  
3    “dark” photon, is a massive particle which couples  
4    weakly to electric charge by mixing with the Standard  
5    Model photon [1]. Consequently, it can be radiated by  
6    electrons and subsequently decay into  $e^+e^-$  pairs, al-  
7   beit at rates far below those of QED trident processes.  
8    Heavy photons have been suggested by numerous be-  
9   yond Standard Model theories [2], to explain the dis-  
10   crepancy between theory and experiment of the muon’s  
11    $g - 2$  [3], and as a possible explanation of recent as-  
12    trophysical anomalies [4, 5, 6]. Heavy photons couple  
13    directly to hidden sector particles with “dark” or “hid-  
14    den sector” charge; these particles could constitute all  
15    or some of the dark matter [7]. Current phenomenology  
16    highlights the  $20 - 1000 \text{ MeV}/c^2$  mass range, and sug-  
17    gests that the coupling to electric charge,  $\epsilon e$ , has  $\epsilon$  in the  
18    range of  $10^{-3} - 10^{-5}$ . This range of parameters makes  
19     $A'$  searches viable in medium energy fixed target elec-  
20    troproduction [8], but requires large data sets and good  
21    mass resolution to identify a small mass peak above the  
22    copious QED background. At small couplings, the  $A'$   
23    become long-lived, so detection of a displaced decay  
24    vertex can reject the prompt QED background and boost  
25    experimental sensitivity.

26    The HPS experiment [9] uses both invariant mass and  
27    secondary vertex signatures to search for  $A'$ . It uses a  
28     $\approx 1 \text{ m}$  long silicon tracking and vertexing detector in-  
29    side a dipole magnet to measure charged particle trajec-  
30    tories and a fast electromagnetic calorimeter just down-  
31    stream of the magnet to provide a trigger and identify  
32    electrons. The experiment utilizes very high-rate front-  
33    end electronics and runs at high trigger rates (up to  
34    50kHz), exploiting the 100% duty cycle of the JLab CE-  
35    BAF accelerator to accumulate the needed statistics.

36    The HPS Test Run, using a simplified version of the  
37    HPS apparatus, was proposed and approved at JLab as  
38    the first stage of HPS. Its purposes included demonstra-  
39    ting that the apparatus and data acquisition systems are  
40    technically feasible and the trigger rates and occupan-  
41    cies to be encountered in electron-beam running are as  
42    simulated. Given dedicated running time with electron  
43    beams, the HPS Test Run apparatus is capable of search-  
44    ing for heavy photons in unexplored regions of parame-  
45    ter space. The key design criteria for HPS and the HPS  
46    Test Run are the same:

- 47    • large and uniform acceptance in the forward region  
48    close to the beam in order to catch boosted  $A'$  de-  
49    cay products,
- 50    • beam passage through the apparatus in vacuum, to

51    eliminate direct interactions with the detector and  
52    minimize beam gas interactions,

- 53    • detector components that can survive and effi-  
54    ciently operate in a high radiation environment  
55    with local doses exceeding 100 Mrad.
- 56    • high-rate electronics with excellent timing resolu-  
57    tion to minimize out of time backgrounds,
- 58    • a flexible, redundant and efficient trigger selecting  
59    electron and positron pairs at rates up to 50 kHz,
- 60    • data handling rates of 100 MB/s to permanent stor-  
61    age,
- 62    • excellent track reconstruction efficiency for elec-  
63    trons and positrons,
- 64    • good angular and momentum resolution to recon-  
65    struct invariant mass precisely,
- 66    • excellent vertex resolution to discriminate dis-  
67    placed  $A'$  decays from prompt QED backgrounds,

68    The HPS Test Run apparatus was installed on April  
69    19, 2012, and ran parasitically in the photon beam of  
70    the HDice experiment [10] until May 18. The JLab  
71    run schedule precluded any dedicated electron beam  
72    running, but the HPS Test Run was allowed a short  
73    and valuable dedicated photon beam run at the end of  
74    scheduled CEBAF running. This final running provided  
75    enough data to demonstrate the functionality of the ap-  
76    paratus, document its performance, and explore trigger  
77    rates, as shown below.

78    This paper reviews the HPS Test Run apparatus, doc-  
79    umenting the performance of the trigger, data acqui-  
80    sition, silicon tracking detector, and the electromag-  
81    netic calorimeter at the level required for calculating the  
82    physics reach of the HPS experiment.

83    **2. Detector Overview**

84    The HPS Test Run apparatus was designed to run  
85    in Hall B at JLab using the CEBAF 499MHz electron  
86    beam at energies between 2.2 and 6.6 GeV and cur-  
87    rents between 200 and 600 nA. The overall design of  
88    the experiment follows from the kinematics of  $A'$  pro-  
89    duction which typically results in a final state particle  
90    within a few degrees of the incoming beam, especially  
91    at low  $m_{A'}$ . Detectors must therefore be placed close  
92    to the beam. The intense electron beam enlarges down-  
93    stream after multiple scattering in the target and elec-  
94    trons which have radiated in the target disperse horizon-  
95    tally in the field of the analyzing magnet. Together they

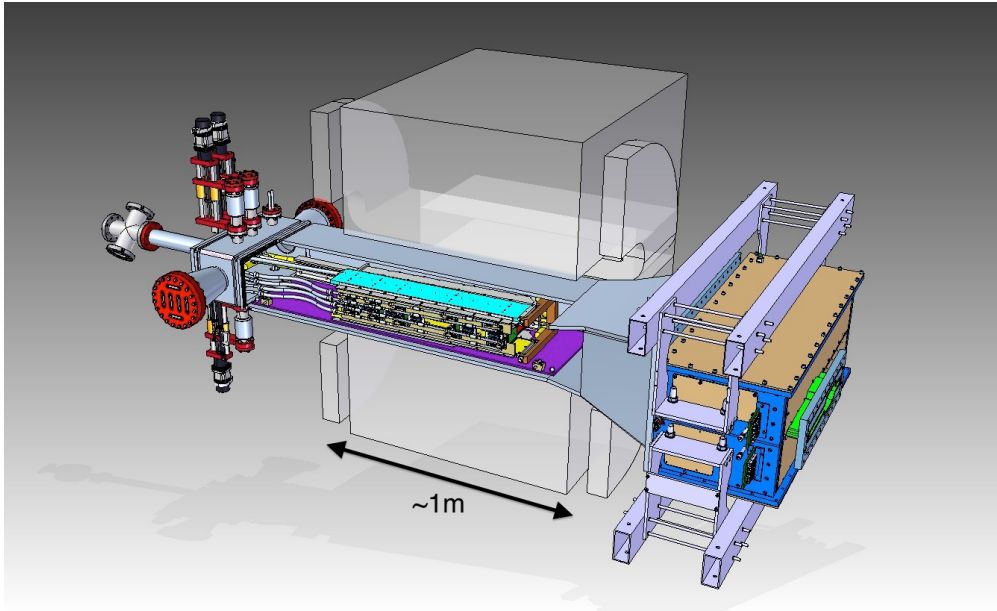


Figure 1: Rendering of the HPS Test Run apparatus installed on the beam line.

96 constitute a “wall of flame” which must be completely  
 97 avoided. Accordingly, the apparatus is split vertically  
 98 to avoid a “dead zone”, the region within  $\pm 15$  mrad of  
 99 the beam plane. In addition, the beam is transported in  
 100 vacuum through the tracker to minimize beam-gas inter-  
 101 action backgrounds. Even with these precautions, the  
 102 occupancies of sensors near the beam plane are high,  
 103 dominated by the multiple Coulomb scattering of the  
 104 primary beam, so high-rate detectors, a fast trigger, and  
 105 excellent time tagging are required to minimize their  
 106 impact. The trigger comes from a highly-segmented  
 107 lead-tungstate ( $\text{PbWO}_4$ ) crystal calorimeter located just  
 108 downstream of the dipole magnet.  
 109

110 A rendering of the apparatus installed on the beam line  
 111 is shown in Figure 1 and an overview of the coverage,  
 112 segmentation and performance is given in Table 1.

113 The silicon tracking and vertexing detector for the  
 114 HPS Test Run, or SVT, resides in a vacuum cham-  
 115 ber inside the Pair Spectrometer (PS) dipole magnet in  
 116 Hall B at JLab. The magnetic field strength was 0.5 T  
 117 oriented vertically throughout the run. The SVT has  
 118 five measurement stations, or “layers,” beginning 10 cm  
 119 downstream of the target. Each layer comprises a pair  
 120 of closely-spaced silicon microstrip sensors respon-  
 121 sible for measuring a single coordinate, or “view”. In-  
 122 troduction of a small (50 or 100 mrad) stereo angle

123 between the two sensors of each layer provides three-  
 124 dimensional tracking and vertexing throughout the ac-  
 125 ceptance of the detector. In order to accommodate the  
 126 dead zone, the SVT is built in two halves that are ap-  
 127 proximately mirror reflections of one another about the  
 128 plane of the nominal electron beam. Each layer in one  
 129 half is supported on a common support plate with inde-  
 130 pendent cooling and readout.  
 131

132 The electromagnetic calorimeter (ECal) is also split  
 133 into two halves. Each half of the ECal consists of  
 134 221  $\text{PbWO}_4$  crystals arranged in rectangular formation.  
 135 There are five rows with 46 modules in each row except  
 136 the row closest to the beam plane which has 37. The  
 137 light from each crystal is read out by an Avalanche Pho-  
 138 todiode (APD) glued on the back surface of the crys-  
 139 tal. Signals from the APDs are amplified using custom-  
 140 made amplifier boards before being sent to the data ac-  
 141 quisition electronics.  
 142

143 The Data Acquisition system combines two architec-  
 144 tures, the Advanced Telecom Communications Archi-  
 145 tecture (ATCA) based SVT readout system and VME-  
 146 bus Switched Serial (VXS) based digitization and trig-  
 147 gering system for the ECal.  
 148

### 3. The HPS Test Run Beamline

149 Since an electron beam was unavailable, the HPS Test  
 150 Run detected the electrons and positrons produced by

Table 1: Overview of the coverage, segmentation and performance of the HPS Test Run detector. The  $\sigma_{d_0}$  is the track impact parameter resolution of the SVT at the nominal electron target position.  $\sigma_{pos}$  is the estimated position resolution perpendicular to the strip direction on the silicon sensors of the SVT.

System	Coverage (mrad)	# channels	ADC (bit)	# layers	Segmentation	Time resolution (ns)	Performance
SVT	$15 < \theta_y < 70$ (5 hits)	12780	14	5 (stereo layers)	$30 \mu\text{m}$ (sense) $60 \mu\text{m}$ (readout) ( $\sigma_{pos} \approx 6 \mu\text{m}$ )	2.5	$\sigma_{d0,y} \approx 100 \mu\text{m}$ $\sigma_{d0,x} \approx 300 \mu\text{m}$ $\sigma_{d0,z} \approx 1 \text{ mm}$
ECal	$15 < \theta_y < 60$	442	12	1	$1.33 \times 1.33 \text{ cm}^2$ $1.6 \times 1.6 \text{ cm}^2$	4 (trigger)	$\sigma(E)/E \approx 4.5\%$

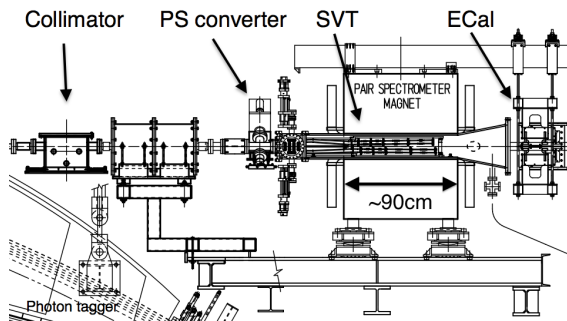


Figure 2: Layout of the HPS parasitic run.

interactions of the secondary photon beam with a thin foil just upstream of the detectors. The HPS Test Run studied the performance of the detectors and the multiple coulomb scattering of the electrons and positrons. Figure 2 shows the layout of the setup on the beam line. The SVT was installed inside the Hall B pair spectrometer magnet vacuum chamber with the ECal mounted downstream of it. Both the SVT and the ECal were retracted off the beam plane compared to nominal electron beam running to allow clean passage of the photon beam through the system.

The photon beam was generated in the interaction of 5.5 GeV electrons with a  $10^{-4} X_0$  gold radiator located  $\approx 9 \text{ m}$  upstream of the PS. The primary beam and scattered electrons are deflected away from detectors by the dipole magnet of the photon tagging system. During the dedicated HPS Test Run period, the collimated (6.4 mm diameter) photon beam passes through the PS pair converter gold foil and later the HPS system. The PS pair converter was located  $\approx 77 \text{ cm}$  upstream of the first layer of the SVT.

Data was taken on three different converter thicknesses with photon fluxes between 0.4 and  $1.3 \times 10^8/\text{s}$  at photon energies between 0.55 and 5.5 GeV produced by a 30 to 90 nA electron beam. Data was measured for both polarities of the PS dipole magnet. The photon beam line during the HPS Test Run produced a rela-

Converter thickn. (% $X_0$ )	Duration (s)	$e^-$ on radiator ( $\mu\text{C}$ )
0	1279	88.1
0.18	2640	193.5
0.45	2149	140.7
1.6	911	24.4

Table 2: Measured integrated currents for the dedicated photon runs.

tively large number of  $e^+e^-$  pairs originating upstream of the converter position. This contribution was measured during data taking with “empty” converter runs, i.e. removing the converter but with all other conditions the same. The runs taken during the time dedicated to HPS Test Run are summarized in Table 2.

#### 4. Silicon Vertex Tracker

The Silicon Vertex Tracker (SVT) enables efficient reconstruction of charged particles and precise determination of their trajectories. This allows  $A'$  decays to be distinguished from background via simultaneous measurements of the invariant mass of  $e^+e^-$  decay products and the position of decay vertices downstream of the target.

The design of the SVT is primarily driven by direct physics requirements and constraints from the environment at the interaction region. The  $A'$  decay products have momenta in the range of 1 GeV/c, so multiple scattering dominates mass and vertexing uncertainties for any possible material budget. The SVT must therefore minimize the amount of material in the tracking volume. The signal yield for long-lived  $A'$  is very small, so the rejection of prompt vertices must be exceedingly pure, on the order of  $10^{-7}$ , in order to eliminate all prompt backgrounds. To achieve the required vertexing performance the first layer of the SVT must be placed no more than about 10 cm downstream of the target. At that distance, it is found that the active region of a sensor can be placed as close as 1.5 mm from the

center of the beam, defining the 15 mrad “dead zone” mentioned previously, to maximize low-mass A’ acceptance with decay products nearly collinear with the beam axis. At the edge of this “dead zone”, the radiation dose approaches  $10^{15}$  electrons/cm<sup>2</sup>/month, or roughly  $3 \times 10^{14}$  1 MeV neutron equivalent/cm<sup>2</sup>/month [11], requiring the sensors to be actively cooled. Meanwhile, very low-energy delta rays from beam-gas interactions would multiply the density of background hits, so the SVT must operate inside the beam vacuum. Finally, in order to protect the sensors, the detector must be movable so that it can be retracted during periods of uncertain beam conditions or beam tuning.

#### 4.1. Layout

The layout of the SVT is summarized in Table 4.1 and rendered in Figure 3. Each of the layers is comprised of a pair of closely-spaced silicon microstrip sensors mounted back-to-back to form a module. A 100 mrad stereo angle is used in the first three layers to provide higher-resolution 3D space points for vertexing. Using 50 mrad in the last two layers breaks the tracking degeneracy of having five identical layers and minimizes fakes from ghost hits to improve pattern recognition. Altogether, the SVT has 20 sensors for a total of 12780 readout channels.

Layer	1	2	3	4	5
<i>z</i> from target (cm)	10	20	30	50	70
Stereo angle (mrad)	100	100	100	50	50
Bend res. ( $\mu\text{m}$ )	$\approx 60$	$\approx 60$	$\approx 60$	$\approx 120$	$\approx 120$
Non-bend res. ( $\mu\text{m}$ )	$\approx 6$	$\approx 6$	$\approx 6$	$\approx 6$	$\approx 6$
# of sensors	4	4	4	4	4
Dead zone (mm)	$\pm 1.5$	$\pm 3.0$	$\pm 4.5$	$\pm 7.5$	$\pm 10.5$
Power cons. (W)	6.9	6.9	6.9	6.9	6.9

Table 3: Layout of the SVT.

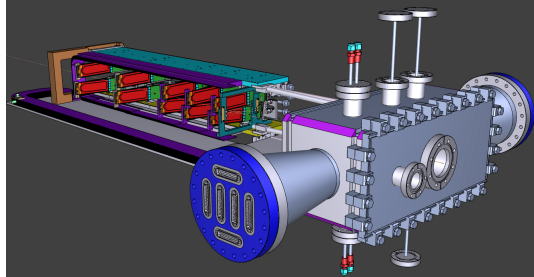


Figure 3: A rendering of the SVT showing the modules on their support plates held by the hinged C-support on the left and the motion levers on the right. The sensors are shown in red and the hybrid readout boards in green. The beam enters from the right through a vacuum box with flanges for services.

The SVT is built in two separate halves that are mirror reflections of one another about the plane of the nominal electron beam. Each half consists of five modules mounted on a support plate that provides services to the modules and allows them to be moved as a group relative to the dead zone. The two halves of the tracker are connected to hinges mounted on a C-shaped support just beyond the last layer that defines the nominal spacing between the upper and lower halves of the tracker. A shaft attached to each support plate in front of layer one extends upstream and connects to a linear shift that transfers motion into the vacuum box through bellows to open and close the two halves around the dead zone. The C-support is mounted to an aluminum baseplate that defines the position of the SVT with respect to the vacuum chamber. Figure 4 shows a photograph of both completed detector halves prior to final assembly.



Figure 4: Both halves of the HPS Test Run SVT after final assembly at SLAC. The cooling manifolds and integrated cable runs are clearly seen.

#### 4.2. Components

The sensors for the SVT are *p*-on-*n*, single-sided, AC-coupled, polysilicon-biased microstrip sensors fabricated on <100> silicon and have 30 (60)  $\mu\text{m}$  sense (readout) pitch over their  $4 \times 10 \text{ cm}^2$  surface. This sensor technology was selected to match the requirement of  $< 1\% X_0$  per layer, single-hit resolution better than 50  $\mu\text{m}$  and tolerance of a radiation dose of approximately  $1.5 \times 10^{14}$  1 MeV neutron equivalent/cm<sup>2</sup> for a six month run. The sensors, produced by Hamamatsu Photonics Corporation, were originally meant for the cancelled Run 2b upgrade of the DØ experiment [12] which satisfied the requirement that the technology must be mature and available within the time and budget constraints.

Despite having only small spots with very high occupancy (up to  $4 \text{ MHz/mm}^2$ ) closest to the primary beam, the rates are still high and lowering the peak occupancy to approximately 1% for tracking requires a trigger window and hit time tagging of roughly 8 ns. The ECal readout and trigger described in Sec. 5.3 can achieve such resolution. To reach this performance the sensors for the SVT are readout by the APV25 ASIC developed for the CMS experiment at CERN [13]. The APV25 can capture successive samples of the shaper output in groups of three at a sampling rate of approximately 40 MHz. By fitting the known *CR-RC* shaping curve to these samples, the initial time of the hit can be determined to a precision of 2 ns for  $S/N \approx 25$  [14]. For electron beam running, six-sample readout and the shortest possible shaping time (35 ns) is used to best distinguish hits that overlap in time. The APV25 ASICs are hosted on simple FR4 hybrid readout boards, outside the tracking volume, with a short twisted-pair pigtail cable to provide power and configuration and signal readout. Along with a single sensor, these are glued to a polyimide-laminated carbon fiber composite backing making up a half-module. A window is machined in the carbon fiber leaving only a frame around the periphery of the silicon to minimize material. A  $50 \mu\text{m}$  sheet of polyamide is laminated to the surface of the carbon fiber with 1 mm overhang at all openings to ensure good isolation between the back side of the sensor, carrying high-voltage bias, and the carbon fiber which is held near ground.

The sensor modules for the SVT consist of a pair of identical half-modules, sandwiched back-to-back around an aluminum cooling block at one end and a similar PEEK spacer block at the other. Figure 5 shows a single module after assembly. The cooling block pro-

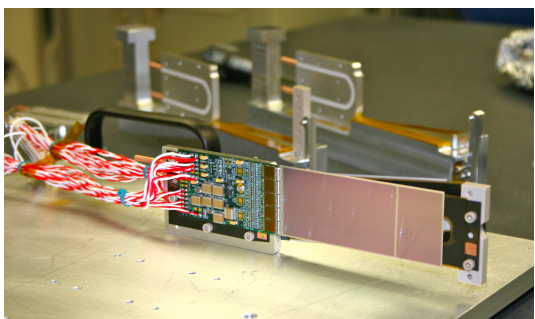


Figure 5: A prototype module assembly (foreground) with the 50 mrad (left) and 100 mrad (right) module assembly fixtures in the background. A pair of cooling blocks and a spacer block can be seen on the fixtures.

vides the primary mechanical support for the module as

well as cooling via copper tubes pressed into grooves in the plates. The spacer block defines the spacing between the sensors at the far end of the module, stiffens the module structure, and improves the stability of the sensor alignment. The average support material in the tracking volume is approximately  $0.06\% X_0$  per double-sided module for a total material budget of 0.7% per layer.

The total SVT power consumption budget of about 50 W is removed by a water/glycol mixture circulated through a flexible manifold attached to the copper tubes in the cooling blocks. During the HPS Test Run the sensors were operated at around  $23^\circ \text{C}$ . The power consumption is dominated by five APV25 ASICs on each hybrid board consuming approximately 2 W, radiant heat load is less than 0.5 W per sensor and leakage current is only significant in a small spot after irradiation.

#### 4.3. Production, Assembly and Shipping

Hybrids with APV25 ASICs underwent quick qualification testing and each half-module was run at low temperature ( $\approx 5^\circ \text{C}$ ) and fully characterized for pedestals, gains, noise and time response after assembly. Of 29 half-modules built, 28 passed qualification testing, leaving eight spare modules after completion of the SVT. Only sensors capable of 1000 V bias voltage without breakdown were used. Full-module assembly and mechanical surveys were performed at SLAC before final assembly, testing and shipping of the SVT to JLab. A custom shipping container with nested crates and redundant isolation for shock and vibration was built in order to safely send the partly assembled SVT to JLab. At JLab, the entire SVT was integrated with the full DAQ and the power supplies before moving the module-loaded support plates to Hall B for final mechanical assembly and installation inside of the vacuum chamber.

#### 4.4. Alignment

The SVT was aligned using a combination of optical, laser and touch probe surveys at SLAC and JLab. The optical survey of individual modules with a precision of a few  $\mu\text{m}$  was combined with a touch-probe survey of the overall SVT support structure, with 25-100  $\mu\text{m}$  precision, to locate the silicon sensor layers with respect to the support plates and the mechanical survey balls on the base plate. After full assembly and installation of the SVT at JLab, a mechanical survey of the SVT base plate position inside the pair spectrometer vacuum chamber is used to determine the global position of the SVT with respect to the CEBAF beam line. The resulting survey-based alignment has the position of the

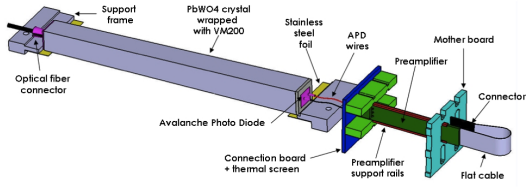


Figure 6: A schematic view of an ECal module.

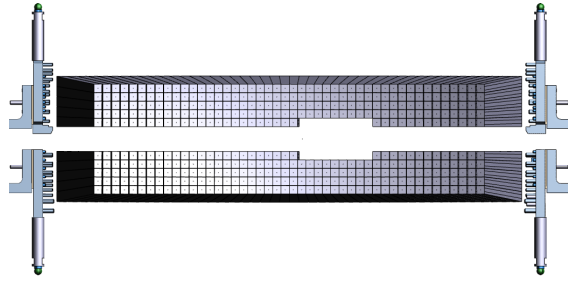


Figure 7: Rendered layout view of the ECal looking downstream.

349 silicon sensors correct to within a few hundred microns  
 350 measured from tracks in the HPS Test Run data. A more  
 351 sophisticated global track-based alignment technique to  
 352 reach final alignment precision well below  $50\text{ }\mu\text{m}$  is be-  
 353 ing developed.

## 354 5. Electromagnetic Calorimeter

355 The electromagnetic calorimeter (ECal), installed  
 356 downstream of the PS dipole magnet, performs two es-  
 357 sential functions for the experiment: it provides a trigger  
 358 signal to select what events to read out from the detector  
 359 sub-systems and is used in the analysis to identify elec-  
 360 trons and positrons. The technology and design choices  
 361 are largely driven by the need for a compact forward de-  
 362 sign covering the SVT A' acceptance and able to fully  
 363 absorb electrons and positrons with energy between 0.5-  
 364 6.5 GeV. It needs granularity and signal readout speed to  
 365 handle  $1\text{ MHz}/\text{cm}^2$  of electromagnetic background and  
 366 to be radiation hard. The PbWO<sub>4</sub> crystal inner calorime-  
 367 ter of the CLAS detector [15, 16, 17], in operation since  
 368 2005 in Hall B, meets all the requirements set by HPS.  
 369 The modules from this calorimeter have been sub-  
 370 sequently repurposed for HPS.

### 371 5.1. Components

372 The ECal module shown in Figure 6 is based on a  
 373 tapered 160 mm long PbWO<sub>4</sub> crystal with a  $13.3 \times$   
 374  $13.3\text{ mm}^2$  ( $16 \times 16\text{ mm}^2$ ) front (rear) face wrapped in  
 375 VM2000 multilayer polymer mirror film. The scintilla-  
 376 tion light, approximately 3 photoelectrons/MeV, is read  
 377 out by a  $5 \times 5\text{ mm}^2$  Hamamatsu S8664-55 Avalanche  
 378 Photodiode (APD) with 75% quantum efficiency glued  
 379 to the rear face surface using MeltMount 1.7 thermal  
 380 plastic adhesive. The low gain of APDs ( $\sim 200$ ) was  
 381 compensated with custom-made preamplifier boards,  
 382 which provide a factor of 2333 amplification of the APD  
 383 signal.

### 384 5.2. Layout

385 Similar to the SVT, the ECal is built in two separate  
 386 halves that are mirror reflections of one another about  
 387 the plane of the nominal electron beam to avoid inter-  
 388 fering with the 15 mrad “dead zone”. As shown in Fig-  
 389 ure 7, the 221 modules in each half, supported by alu-  
 390 minum support frames, are arranged in rectangular for-  
 391 mation with five layers and 46 crystals/layer except for  
 392 the layer closest to the beam where nine modules were  
 393 removed to allow a larger opening for the outgoing elec-  
 394 tron and photon beams. Each half was enclosed in a  
 395 temperature controlled box ( $< 1^\circ\text{ F}$  stability and  $< 4^\circ\text{ F}$   
 396 uniformity) to stabilize the crystal light yield and the op-  
 397 eration of the APDs and its preamplifiers. Four printed  
 398 circuit boards mounted on the backplane penetrated the  
 399 enclosure and were used to supply the  $\pm 5\text{ V}$  operating  
 400 voltage for the preamplifiers, 400 V bias voltage to the  
 401 APDs, and to read out signals from the APDs. Each half  
 402 of the ECal was divided into 12 bias voltage groups with  
 403 a gain uniformity of about 20%.

404 During the HPS Test Run, both halves were held in  
 405 place by four vertical bars attached to a rail above, plac-  
 406 ing the front face of the crystals 147 cm from the up-  
 407 stream edge of the magnet, with a 8.7 cm gap between  
 408 the innermost edge of the crystals in the two halves.

### 409 5.3. Signal readout

410 After a 2:1 signal splitter, 1/3 of an amplified APD  
 411 signal was fed to a single channel of a JLab flash ADC  
 412 (FADC) board [18]. 2/3 of the signal was sent to a  
 413 discriminator module and then to a TDC for a timing  
 414 measurement. The FADC boards are high speed VXS  
 415 modules digitizing up to 16 APD signals at 250 MHz  
 416 and storing samples in 8  $\mu\text{s}$  deep pipelines with 12-bit  
 417 resolution. When a trigger is received, the part of the  
 418 pipeline from 5 samples before and 30 after the signal  
 419 which crossed a programmable threshold (for the HPS  
 420 Test Run this was set to  $\approx 70\text{ MeV}$ ) are summed and

421 stored in a 17-bit register for readout. In addition a  
 422 4 ns resolution timestamp of the threshold crossing is  
 423 reported in the readout for each pulse. This scheme  
 424 significantly compresses the data output of the FADC.  
 425 During offline data analysis, a calibrated pedestal value  
 426 is subtracted to obtain the actual summed energy. Two  
 427 20-slot VXS crates with 14 (13) FADC boards were em-  
 428 ployed in the HPS Test Run to read out the top (bottom)  
 429 half of the ECal. In the HPS Test Run 385 out of 442  
 430 modules (87%) were used in offline reconstruction, 39  
 431 modules were disabled or not read out (no FADC chan-  
 432 nel available, no APD bias voltage or masked out due  
 433 to excessive noise) and 18 were masked offline due to  
 434 noise.

## 435 6. Trigger and Data Acquisition

436 The DAQ system handles acquisition of data from the  
 437 ECal and SVT sub-detectors with two DAQ architec-  
 438 tures. The SVT DAQ is based on Advanced Telecom  
 439 Communications Architecture (ATCA) hardware while  
 440 the ECal uses VMEbus Switched Serial (VXS) based  
 441 hardware. Data from the sub-detectors are only read  
 442 out when a trigger signal from the trigger system is re-  
 443 ceived.

### 444 6.1. Trigger system

445 The trigger system is designed to select time coinci-  
 446 dences of electromagnetic clusters in the top and bot-  
 447 tom halves of the ECal. Figure 8 shows a schematic  
 448 overview of each stage of the system. Each channel on  
 449 the FADC board has an independent data path to send 5-  
 450 bit pulse energy and 3-bit pulse arrival time information  
 451 every 32 ns to a trigger processing board (CTP), which  
 452 is in the same crate. The 3-bit pulse arrival time allows  
 453 the trigger to know the pulse timing at 4 ns resolution.  
 454 Contrary to the readout path described in Sec. 5.3, this  
 455 energy is a pedestal-subtracted time-over-threshold sum

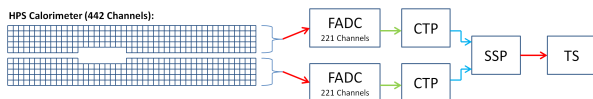


Figure 8: Block diagram of the ECAL trigger system consisting of the FADC that samples and digitizes signals for each detector channel and sends them for cluster finding in the CTP. The CTP clusters are sent to the SSP where the final trigger decision is taken based on pairs of clusters in both halves of the ECal. The decision is sent to the Trigger Supervisor (TS) that generates the necessary signals to read out the sub-detectors.

with programmable offsets and minimum threshold dis-  
 457 criminator for each channel. With input from all FADC  
 458 channels, i.e. one half of the ECal, the CTP performs  
 459 cluster finding and calculates cluster energy and tim-  
 460 ing information. The 3x3 fixed-window, highly parallel,  
 461 FPGA-based cluster algorithm simultaneously searches  
 462 for up to 125 clusters with energy sum larger than the  
 463 programmable energy threshold ( $\approx 270$  MeV). Crystals  
 464 in the fixed-window are included in the sum if the lead-  
 465 ing edge of the pulse occurred within a 32 ns time win-  
 466 dow to take into account clock skew and jitter through-  
 467 out the system. The CTP only accepts clusters with the  
 468 locally highest energy 3x3 window to deal with over-  
 469 lapping and very large clusters. The sub-system board  
 470 (SSP) receives the clusters from the top and bottom half  
 471 CTP at a maximum of 250MHz and searches for pairs  
 472 of clusters in an 8 ns wide coincidence window. The  
 473 SSP sends triggers to the trigger supervisor (TS), which  
 474 generates all the necessary signals and controls the en-  
 475 tire DAQ system readout through the trigger interface  
 476 units installed in every crate that participate in the read-  
 477 out process.

The trigger system is free-running and driven by the  
 478 250 MHz global clock and has essentially zero dead  
 479 time at the occupancies expected for HPS. The trigger  
 480 supervisor can apply dead time if necessary, for exam-  
 481 ple on a ‘busy’ or ‘full’ condition from the front-end  
 482 electronics. The system is designed to handle trigger  
 483 rates above 50 kHz and has a latency set to  $\approx 3 \mu\text{s}$  to  
 484 match that required by the SVT APV25 ASIC. During  
 485 the HPS Test Run, for the most part the trigger system  
 486 required only a single cluster in either the top or bot-  
 487 tom ECal halves and was tested to trigger rates above  
 488 100 kHz by lowering thresholds.

### 490 6.2. SVT Data Acquisition

The SVT DAQ is based on the Reconfigurable Clus-  
 491 ter Element (RCE) and cluster interconnect concept de-  
 492 veloped at SLAC as generic building blocks for DAQ  
 493 systems. The RCE is a generic computational build-  
 494 ing block, housed on a separate daughter card called  
 495 Data Processing Module (DPM), that is realized on an  
 496 ATCA front board called the Cluster On Board (COB),  
 497 see Figure 9. The first generation RCE used in the HPS  
 498 Test Run consisted of a Virtex 5 FPGA with 1 GB of  
 499 DDR3 RAM. A schematic overview of the system is  
 500 shown in Figure 10. The analog outputs of up to 12  
 501 SVT half-modules (60 APV25 ASICs) are digitized on  
 502 the Rear-Transition-Module (RTM), a custom board on  
 503 the back side of the ATCA crate, interfacing the HPS-  
 504 specific readout to the generic DAQ components on the  
 505 COB. A pre-amplifier converts the APV25 differential



Figure 9: The SVT DAQ COB board with four data processing daughter cards (DPMs) visible on the left side.

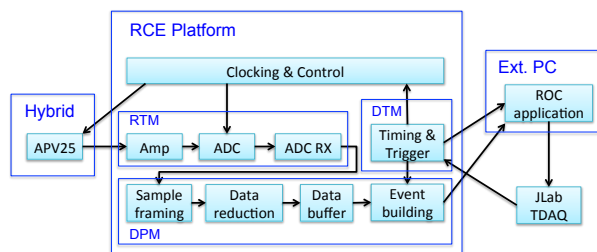


Figure 10: Block diagram overview of the SVT DAQ.

current output to a different voltage output scaled to the sensitive range of a 14-bit ADC operating at the system clock of 41.667 MHz. The RTM is organized into four sections with each section supporting three SVT half-module hybrids (15 APV25 ASICs). The RTM also includes a 4-channel fiber-optic module and supporting logic which is used to interface to the JLab trigger system supervisor. Each section of the RTM is input to a DPM which applies thresholds for data reduction and organizes the sample data into UDP datagrams. The DPM also hosts an I<sup>2</sup>C controller used to configure and monitor the APV25 ASICs. A single ATCA crate with two COB cards was used, one supporting four DPMs and one supporting three DPMs and one DPM that is configured as the trigger and data transmission module. The two COB cards and their DPMs are interconnected with a 10 Gb/s switch card [19] which also hosts two 1Gb/s Ethernet interfaces to the external SVT DAQ PC.

The external PC supports three network interfaces: two standard 1 Gb/s Ethernet and one custom low-latency data reception card. The first is used for slow control and monitoring of the 8 DPM modules and the second serves as the interface to the JLAB data acquisition system. The third custom low-latency network interface is used to receive data from the ATCA crate and supports a low latency, reliable TTL trigger acknowl-

edge interface to the trigger DPM. This PC hosts the SVT control and monitoring software as well as the Read Out Controller application used to interface with the JLab DAQ.

In order to minimize cable length for the analog APV25 output signal the ATCA crate was located approximately 1 m from the beam line, next to our cable vacuum feed-throughs. Before shielding with lead-blankets was arranged, we observed two failures of normally reliable ATCA crate power supplies, time-correlated to beam instabilities.

Although trigger rates during the HPS Test Run were significantly lower, this system was tested at trigger rates up to 20 kHz and 50 MB/s. With optimized event blocking and improved ethernet bandwidth, together with utilizing the overlapping readout and trigger functionality of the APV25, the system is capable of being read out at 50 kHz trigger rate.

### 6.3. General Data Acquisition and Online Computing

Every crate participating in the readout process contains a Readout Controller (ROC) that collects digitized information, processes it, and sends it on to the event builder. For the ECal, both VXS crates run ROC applications in a single blade Intel-based CPU module running CentOS Linux OS. For the SVT DAQ, the ROC application runs on the external PC under RHEL. The event builder assembles information from the ROCs into a single event which is passed to the event recorder that writes it to a RAID5-based data storage system capable of handling up to 100 MB/s. The event builder and other critical components run on multicore Intel-based multi-CPU servers. The DAQ network system is a network router providing 10 Gb/s high-speed connection to the JLab computing facility for long-term storage. For the HPS Test Run, both the SVT and ECal ROC had a 1 Gb/s link to the network router.

## 7. Reconstruction and Performance

### 7.1. SVT Performance

For the duration of the HPS Test Run all SVT modules and APV25 chips were configured to their nominal operating points [20] with all sensors reverse-biased at 180 V. The sensors were operated within a temperature range of 20 – 24°C. Approximately 97% of the 12,780 SVT channels were found to be operating normally; the fraction of dead or noisy channels varied from 2.4% to 4.7% throughout the HPS Test Run. Most of these losses were due to 2-4 misconfigured APV25 ASICs, a known noisy half-module and problems in two particular APV25 ASICs.

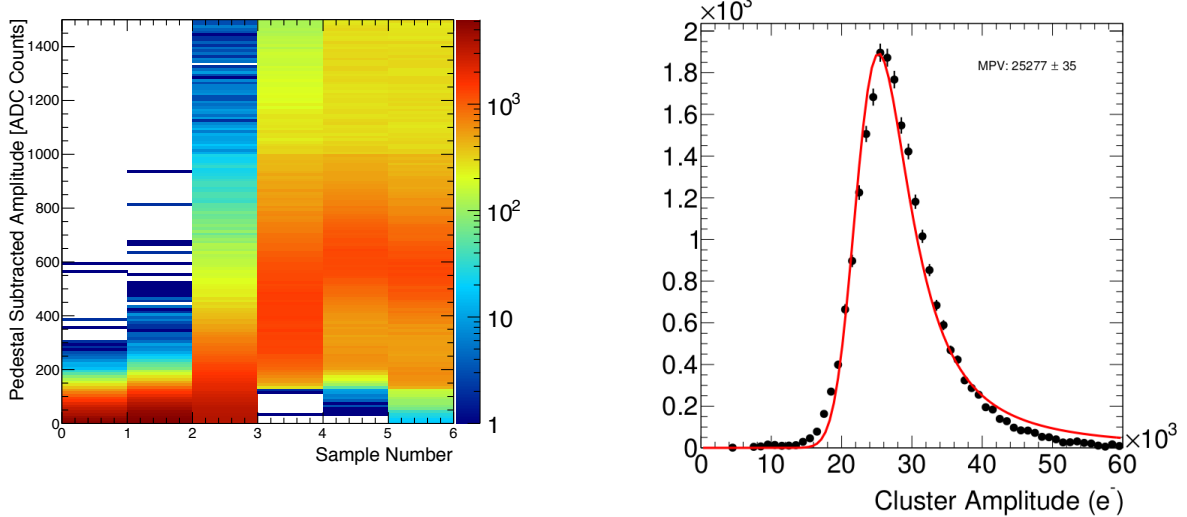


Figure 11: Accumulation of six pedestal-subtracted samples from individual SVT channels associated with hits on tracks.

Figure 12: The cluster charge distribution for hits associated with a track follow the characteristic Landau shape.

### 582 7.1.1. Cluster and Hit Reconstruction

583 After a trigger is received, the amplitude of every  
 584 APV25 analogue output is sampled and digitized in six  
 585 consecutive time bins, separated by roughly 25 ns. A  
 586 data reduction algorithm is applied requiring three out  
 587 of six samples to be above two times the noise level and  
 588 that the third sample is larger than the second or that  
 589 the fourth sample is larger than the third. The typical,  
 590 pedestal subtracted, pulse shape obtained is shown in  
 591 Figure 11. As the figure demonstrates, the SVT was  
 592 well timed-in to the trigger with the rise of the pulse at  
 593 the 3rd sampling point. In order to find the time,  $t_0$ , and  
 594 amplitude of each hit, the six samples from each chan-  
 595 nel are fitted to an ideal  $CR - RC$  function. Note that  
 596 in the HPS Test Run the APV25 ASICs were operating  
 597 with a 50 ns shaping time. These hits are passed through  
 598 a simple clustering algorithm which forms clusters by  
 599 grouping adjacent strips with the position of a cluster on  
 600 the sensor determined by the amplitude-weighted mean.  
 601 With a linear gain up to  $\approx 3$  MIPs, the cluster charge  
 602 for hits associated with a track follow the characteris-  
 603 tic Landau shape, see Figure 12. A noise level between  
 604  $1.1 - 1.5 \times 10^3$  electrons was established through multiple  
 605 calibration runs giving a signal to noise ratio of  $21 - 25$ .  
 606 Lab-based radioactive source tests were used to provide  
 607 the absolute charge normalization. After clustering hits  
 608 on a sensor, the hit time for each cluster is computed as  
 609 the amplitude-weighted average of the individually fit-  
 610 ted  $t_0$  on each channel. The  $t_0$  resolution is studied by  
 611 comparing the cluster hit time with the average of all

612 cluster hit times on the track shown in Figure 13. After  
 613 correcting for offsets from each sensor (time-of-flight  
 614 and clock phase) and accounting for the correlation be-  
 615 between the  $t_0$  and track time, the extracted  $t_0$  resolution is  
 616 2.6 ns. This is somewhat worse than the approximately  
 617 2 ns resolution expected for S/N=25 which we attribute  
 618 to the true pulse shape differing from our idealized fit  
 619 function which will be improved in the future [21]. Re-  
 620 ducing the APV25 ASIC pulse shaping time to 35 ns  
 621 will also improve time resolution. These results show  
 622 that we can operate with the six sample readout mode  
 623 of the APV25 chip and achieve time resolution adequate  
 624 for pileup rejection during electron running in HPS.

625 Good agreement was obtained between observed and  
 626 simulated occupancies after taking into account dead or  
 627 noisy channels. The hit reconstruction efficiency was  
 628 estimated by measuring the number of good tracks with  
 629 a hit close to the extrapolated intersection of a given  
 630 sensor that was excluded from the track fit itself. Tracks  
 631 which intersect regions with known bad channels or  
 632 pass very close to the edge region were excluded. The  
 633 hit reconstruction efficiency, see Figure 14, was mea-  
 634 sured to be above 98% and fairly uniform across the  
 635 SVT.

636 The spatial resolution of similar microstrip sensors is  
 637 well established by test beam data, against which the  
 638 charge deposition model in the simulation is validated.  
 639 This resolution can be parameterized as a function of the  
 640 total signal to single-strip noise and the crossing angle  
 641 of tracks through the sensor. The single-hit resolution

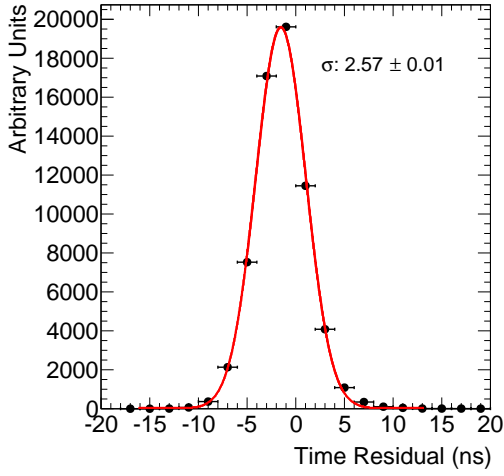


Figure 13: The residual of individual cluster times with the average of all clusters on the track.

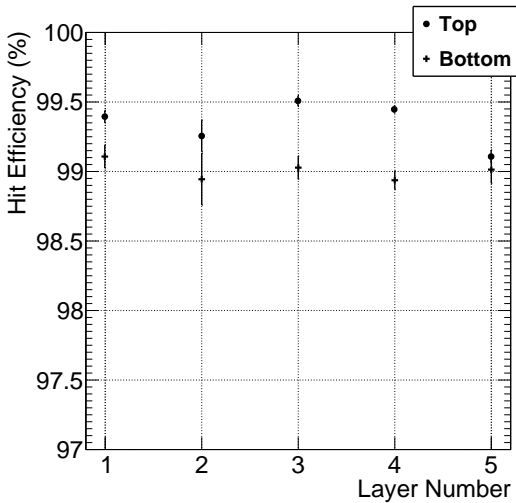


Figure 14: The hit reconstruction efficiency as a function of detector layer.

for charged particles with signal-to-noise ratio above 20, as demonstrated here, is relatively constant at approximately 6  $\mu\text{m}$  for tracks that enter approximately normal to the sensors as in HPS.

#### 7.1.2. Momentum and Vertexing Resolution

By selecting  $e^+e^-$  pairs from the triggered events we are able to study basic distributions of pair production kinematics. Pairs of oppositely charged tracks, one in the top and one in the bottom half of the SVT, with momentum larger than 400 MeV were selected. The pair production kinematics are relatively well reproduced as shown in Figure 15.

The expected momentum resolution from simulation is between 4-5% for tracks in the momentum range of the HPS Test Run. By comparing, between data and simulation, the shapes of the kinematic distributions for single- and two-track events, we estimate an agreement with the nominal scale and resolution to within 10%.

In the HPS Test Run, as well as in electron running with HPS, the dominant source of uncertainty in the tracking and vertexing is multiple Coulomb scattering. For the vertexing performance the foremost difference compared to electron beam running is that the target was located approximately 67 cm upstream from our nominal target position; giving almost collinear tracks in the detector. The increased lever arm over which tracks are extrapolated widens the resolution with up to a factor of eight (depending on momentum) compared to what is achieved at the nominal electron target position for HPS. Figure 16 shows the horizontal and vertical positions of the extrapolated track at the converter position. While residual alignments show small shifts, the good agreement between data and simulated events of the widths indicates a good understanding of the material budget and distribution in the SVT. Having the dominant contribution to the vertex resolution approximately right demonstrates that the resolution in HPS, with a target at 10 cm, will be as calculated.

#### 7.2. ECal Performance

The integrated pulse of each FADC channel was converted to energy by subtracting a pedestal and applying a conversion factor to convert ADC counts to energy. The pedestals are measured using special runs where each trigger records 100 samples of signals from the APDs with 4 ns between each sample. The pedestals were extracted from the part of the window before the actual hit in the calorimeter. Modules with signal above

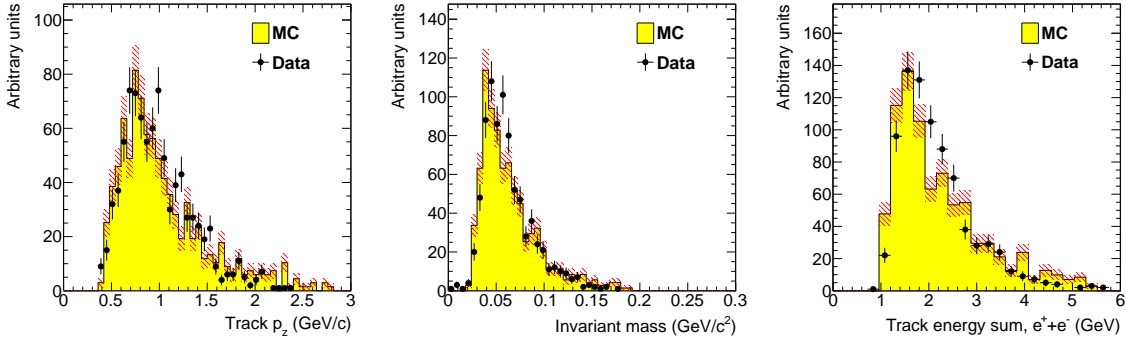


Figure 15: Kinematic distributions for  $e^+e^-$  pairs selected by opposite charged tracks in the top and bottom half of the tracker: track momentum in the top half of the SVT (left), invariant mass (middle) and the sum of the track energy for the pair (right).

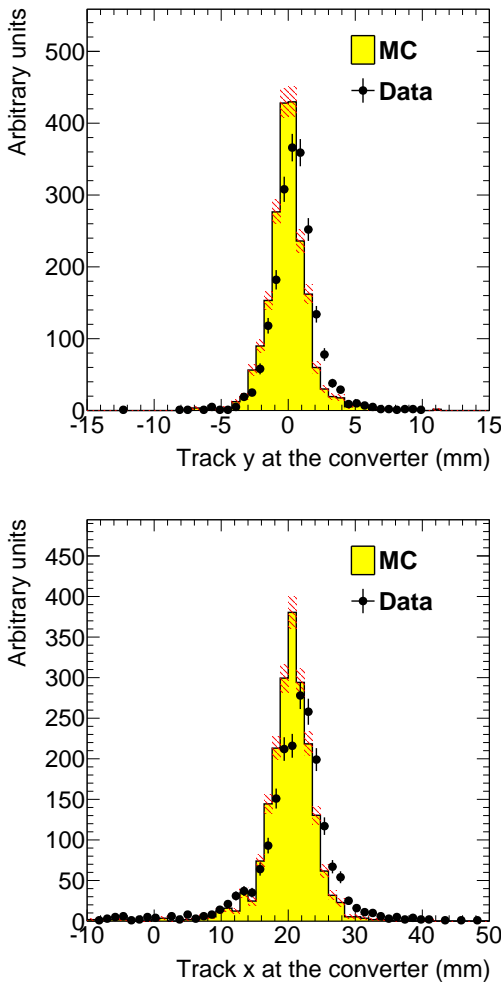


Figure 16: Vertical (top) and horizontal (bottom) extrapolated track position at the converter taking into account the measured fringe field.

the threshold are clustered using a simple algorithm similar to the one deployed for the trigger (see Sec. 6.1). Due to the high effective readout threshold of 73 MeV the average number of crystals in a cluster was  $\sim 3$  and the simple clustering algorithm worked well for reconstruction of the detected shower energy. An average noise level of approximately 15 MeV was measured in special pedestal runs.

The ratio of the ECal cluster energy  $E$  to the momentum  $p$  of a matched track in the SVT was used to determine the conversion factors from ADC counts to energy. To compare data and simulation, all inoperable or noisy channels in the SVT and ECal were disabled in both data and simulation so that any efficiency or bias that affect the data should be reflected in the simulation. Iteratively, conversion coefficients for each crystal were adjusted until the  $E/p$  ratio in data and simulation were similar. The distribution of the  $E/p$  ratio in data and simulation are compared in Figure 17. The peak position of the distribution indicates the sampling fraction of the ECal, the fraction of the incident particle energy measured in the cluster. The width and tails of the distribution in data indicates imperfect calibration and noise of the ECal modules. This level of calibration and the agreement with simulation was found to be sufficient to study normalized event rates in the HPS Test Run.

### 7.3. Trigger Performance

As described above in Sec. 6, the energy from each crystal is measured differently in the trigger and what is readout from the ECal. The trigger performance was studied by simulating the trigger for each event and comparing to how the events were actually triggered. To eliminate trigger bias, we use a tag and probe method: to study the trigger performance in one half of the ECal, we select events which triggered the other

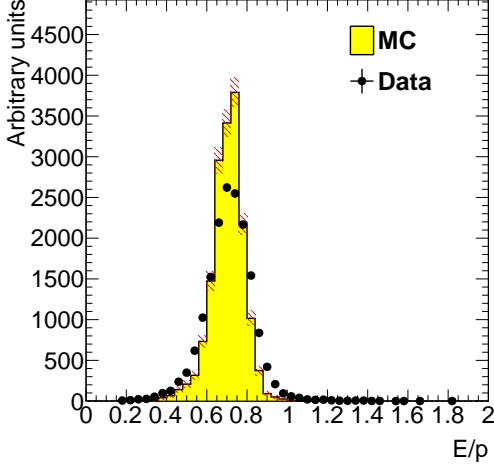


Figure 17: The ECal energy over track momentum ratio ( $E/p$ ) comparing data and simulation for single cluster triggers in the top half of the ECal.

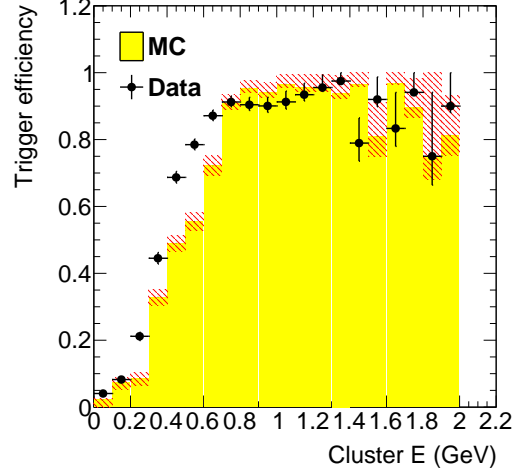


Figure 18: Trigger efficiency in both halves of the ECal for data and simulation as a function of cluster energy.

half and where there was exactly one probe cluster in the ECal half under study. We then measure trigger efficiency as the fraction of tagged events that fired the trigger in the probe half as a function of the probe cluster energy, shown in Figure 18. The trigger turn-on is slow and reaches an uneven plateau at about 700 MeV for two reasons; gain variations between different crystals lead to the threshold variations and the nonlinearity of the time-over-threshold integral means that the effective threshold is higher for clusters that span multiple crystals. The effective trigger threshold is therefore dependent on position and energy of the particle as well as cluster multiplicity.

As a cross-check we simulate the FADC trigger path by converting from readout hits (with fixed-size window integration) to trigger hits (time-over-threshold integration). The CTP clustering algorithm and the trigger decision from the SSP are simulated before we compare the trigger decision and trigger time to what was reported by the actual trigger. For every event, the trigger reports the trigger decision as a bit mask (top half, bottom half or both) and the time the trigger fired. The turn-on from the trigger threshold was measured to be 1280 in units of ADC counts as expected. The threshold was not perfectly sharp because of uncertainties in the conversion from readout to trigger hits described above, but based on comparisons with simulation we found that the trigger worked exactly as specified.

Converter (% $X_0$ )	<b>1.60</b>	<b>0.45</b>	<b>0.18</b>
EGS5	$1162 \pm 112$	$255 \pm 28$	$94 \pm 17$
Geant4	$2633 \pm 250$	$371 \pm 38$	$114 \pm 18$
Observed	$1064 \pm 2$	$196 \pm 1$	$92 \pm 1$

Table 4: Observed and predicted event rate (in Hz) normalized to 90 nA for three different converter thicknesses. The uncertainty on the prediction includes systematic uncertainties from ECal alignment, background normalization, beam current normalization and limited statistics in the simulation.

#### 7.4. Trigger Rate Comparisons

Trigger rates observed in the HPS Test Run are dominated by multiple Coulomb scattered  $e^+e^-$  pairs in the converter. In simulated events, the rate of triggers depend on the modeling of the pairs' angular distribution and the subsequent multiple Coulomb scattering in the converter. Rates from different converter thicknesses are used to study the varying multiple Coulomb scattering contribution (pair production angular distribution is constant), and are compared with Geant4 [22] standard multiple scattering model and EGS5 [23]. Restricting clusters to a well calibrated region of the ECal and subtracting the “no converter” background we see agreement with the rates predicted by the EGS5 simulation program, see Table 7.4. This gives further confidence that the dominant source of background occupancy for HPS, multiple Coulomb scattered beam electrons, is well described.

771 **8. Summary and Outlook**

772 The HPS Test Run experiment, using a simplified  
773 version of the apparatus planned for the full HPS ex-  
774 periment in a parasitic photon beam, demonstrated the  
775 feasibility of the detector technologies proposed for  
776 the silicon vertex tracker, electromagnetic calorimeter,  
777 and data acquisition systems. Performance from each  
778 of these subsystems has been shown to be adequate  
779 to conduct the full experiment successfully. Studies  
780 of multiple Coulomb scattering tails of electrons and  
781 positrons from photon conversions further backs ex-  
782 pectations from simulation, giving credence to estimates  
783 of the detector backgrounds expected in electron beam  
784 running for HPS.

785 **9. Acknowledgements**

786 The authors are grateful for the support from Hall B  
787 at JLab and especially the Hall B engineering group for  
788 support during installation and decommissioning. They  
789 also would like to commend the CEBAF personnel for  
790 good beam performance, especially the last few hours  
791 of operating CEBAF6. The tremendous support from  
792 home institutions and supporting staff also needs praise  
793 from the authors.

794 This work has been supported by the US Department  
795 of Energy.

796 **References**

- [1] B. Holdom, Two U(1)'s and Epsilon Charge Shifts, *Phys.Lett.* B166 (1986) 196.
- [2] R. Essig, J. A. Jaros, W. Wester, P. H. Adrian, S. Andreas, et al., Dark Sectors and New, Light, Weakly-Coupled Particles, Report of the Community Summer Study 2013 (Snowmass) Intensity Frontier New, Light, Weakly-Coupled Particles subgroup (2013).
- [3] M. Pospelov, Secluded U(1) below the weak scale, *Phys.Rev.* D80 (2009) 095002.
- [4] O. Adriani, et al. (PAMELA Collaboration), An anomalous positron abundance in cosmic rays with energies 1.5-100 GeV, *Nature* 458 (2009) 607–609.
- [5] M. Ackermann, et al. (Fermi LAT Collaboration), Measurement of separate cosmic-ray electron and positron spectra with the Fermi Large Area Telescope, *Phys.Rev.Lett.* 108 (2012) 011103.
- [6] M. Aguilar, et al. (AMS Collaboration), First Result from the Alpha Magnetic Spectrometer on the International Space Station: Precision Measurement of the Positron Fraction in Primary Cosmic Rays of 0.5350 GeV, *Phys.Rev.Lett.* 110 (2013) 141102.
- [7] N. Arkani-Hamed, D. P. Finkbeiner, T. R. Slatyer, N. Weiner, A Theory of Dark Matter, *Phys.Rev.* D79 (2009) 015014.
- [8] J. D. Bjorken, R. Essig, P. Schuster, N. Toro, New Fixed-Target Experiments to Search for Dark Gauge Forces, *Phys.Rev.* D80 (2009) 075018.
- [9] A. Grillo, et al. (HPS Collaboration), Heavy Photon Search Proposal, 2010. URL: <https://confluence.slac.stanford.edu/download/attachments/866767>
- [10] A. Sandorfi, et al., 2012. URL: [http://www.jlab.org/exp\\_prog/proposals/06/PR-06-101.pdf](http://www.jlab.org/exp_prog/proposals/06/PR-06-101.pdf).
- [11] I. Rashevskaya, S. Bettarini, G. Rizzo, L. Bosisio, S. Dittongo, et al., Radiation damage of silicon structures with electrons of 900-MeV, *Nucl.Instrum.Meth.* A485 (2002) 126–132.
- [12] D. S. Denisov, S. Soldner-Rembold, D0 Run IIB Silicon Detector Upgrade: Technical Design Report (2001).
- [13] M. French, L. Jones, Q. Morrissey, A. Neviani, R. Turchetta, et al., Design and results from the APV25, a deep sub-micron CMOS front-end chip for the CMS tracker, *Nucl.Instrum.Meth.* A466 (2001) 359–365.
- [14] M. Friedl, C. Irmel, M. Pernicka, Readout of silicon strip detectors with position and timing information, *Nucl.Instrum.Meth.* A598 (2009) 82–83.
- [15] F.-X. Girod, M. Garon (CLAS), Inner calorimeter in clas/dvcs experiment, CLAS-Note 2005-001 (2005).
- [16] R. Niyazov, S. Stepanyan (CLAS), Clas/dvcs inner calorimeter calibration, 2005. URL: <https://misportal.jlab.org/u1/Physics/Hall-B/clas/>.
- [17] F.-X. Girod (Université de Strasbourg), 2006. URL: <http://www.jlab.org/Hall-B/general/thesis/fxgirod.pdf>.
- [18] H. Dong, et al., Integrated tests of a high speed VXS switch card and 250 MSPS flash ADCs, 2007. doi:10.1109/NSSMIC.2007.4436457.
- [19] R. Larsen, Emerging New Electronics Standards for Physics, *Conf.Proc.* C110904 (2011) 1981–1985.
- [20] L. Jones, APV25-S1: User guide version 2.2, RAL Microelectronics Design Group, 2011.
- [21] M. Friedl, C. Irmel, M. Pernicka, Obtaining exact time information of hits in silicon strip sensors read out by the {APV25} front-end chip, Nuclear Instruments and Methods in Physics Research Section A: Accelerators, Spectrometers, Detectors and Associated Equipment 572 (2007) 385 – 387. Frontier Detectors for Frontier Physics Proceedings of the 10th Pisa Meeting on Advanced Detectors.
- [22] S. A. et al., Geant4 simulation toolkit, *Nucl.Instrum.Meth.* A506 (2003) 250 – 303.
- [23] H. Hirayama, Y. Namito, A. Bielajew, S. Wilderman, W. Nelson, The EGSS Code System, 2005.
- [24] D. Attwood, P. Bell, S. Bull, T. McMahon, J. Wilson, et al., The scattering of muons in low Z materials, *Nucl.Instrum.Meth.* B251 (2006) 41–55.
- [25] G. Shen, C. Ankenbrandt, M. Atac, R. M. Brown, S. Ecklund, et al., Measurement of Multiple Scattering at 50-GeV/c to 200-GeV/c, *Phys.Rev.* D20 (1979) 1584.
- [26] B. Gottschalk, A. Koehler, R. Schneider, J. Sisterson, M. Wagner, Multiple coulomb scattering of 160 mev protons, Nuclear Instruments and Methods in Physics Research Section B: Beam Interactions with Materials and Atoms 74 (1993) 467 – 490.